Deep Mining 2024 – P Andrieux & D Cumming-Potvin (eds)

doi:10.36487/ACG_repo/2465_40

Rockburst assessment and control: a case study of a deep sill pillar recovery

Carlos Rojas Perez [a,*], Wei Wei [b], Alec Gilvesy [b], Felicity-Jayne Borysenko [b], Hani S Mitri [a]

[a] *Department of Mining Engineering, McGill University, Canada*

[b] *Agnico Eagle Mines, Canada*

Abstract

Rockburst control in deep mining is a challenging problem, especially in high extraction ratio zones. The increased likelihood of rockburst occurrence can be a cause of safety concerns for the mine operators. The parameters associated with rockbursts are generally related to geological features, rock properties, seismic activities and the mining rate. Mining aspects such as mining sequence, mining direction, stope geometry, backfill selection and the mining method all contribute to the occurrence of rockburst. This study demonstrates a stepwise methodology for the assessment and safe recovery of a sill pillar at Agnico Eagle Mines Ltd's Macassa mine. The pillar is situated 1,700 m (5,600 ft) below surface. It is 110 m (360 ft) long and 15.5 m (50 ft) in height, with a varying thickness averaging 3 m (10 ft). The sill pillar is planned for extraction with longhole stoping in retreat. Past mining activities employed the cut-and-fill method; the levels above and below the sill pillar are tight-filled with paste fill. To assess the stress condition in the pillar, a 3D mine-wide numerical model was created with FLAC3D finite difference code. The numerical model employs the Macassa geomechanical database and in situ stress regime. Pillarburst conditions are assessed using the deviatoric stress ratio to estimate potential brittle shear failure, and the burst potential index based on energy considerations to examine strainburst potential. Model calibration relies on microseismic monitoring activities in the sill pillar over the past year. Rockburst mitigation and control methods with dynamic supports in the sill drives are discussed.

Keywords: *rockburst, sill pillar, numerical modelling, rockburst control, pillar recovery, deep mining*

1 Introduction

Rockburst is one of the most challenging phenomena encountered in underground mines and is characterised by sudden and violent failures of rock masses (Ortlepp 1997). Over the years numerous studies have linked rockbursts to energy release (Blake 1972; Gill et al. 1993; He et al. 2007), brittle rock properties (He 2005; Solak 2009) and seismic activities (Hedley 1992; Blake & Hedley 2003). A critical aspect in understanding and assessing rockburst lies in its classification, which captures pertinent information about these occurrences. Various classification systems have been proposed with a variety of properties to represent the different types of events which occur underground.

Kaiser et al. (1996) based their classification on the types of rockburst damage mechanisms and damage severity. He et al. (2012) reported a classification defined by the triggering mechanism with the support of laboratory data. They based their classification on a series of tests simulating the conditions in deep mining. The early classification proposed by Ortlepp (1992) is the first one to relate the seismic event type to the source mechanism, first motion seismic records and event magnitude (Table 1).

* Corresponding author.

Table 1 Classification of rockburst types proposed by Ortlepp (1992)

Seismic event	Postulated source mechanism	First motion seismic records	Richter magnitude ML
Strainbursting	Superficial spalling with violent ejections of fragments	Usually undetected, could be implosive	–0.2 to 0
Buckling	Outward expulsion of larger slabs pre-existing parallel to opening	Implosive	0 to +1.5
Pillar or face crush	Violent expulsion of rock from tunnel face or pillar	Implosive	+1.0 to +2.5
Shear rupture	Violent propagation of shear fracture through intact rock mass	Double-couple shear	+2.0 to +3.5
Fault slip	Violent renewed movement on existing fault	Double-couple shear	+2.5 to +5.0

Another relevant topic to address regarding rockbursts is their causes. Kaiser & Cai (2018) proposed to categorise the causes for rockbursts into four main groups: geotechnical, geologic, mining and seismic-related parameters. However, it can be argued that seismic activities are a natural companion to rockburst occurrence; thus they cannot be defined as an independent cause for rockburst events. Therefore, leaving aside the events which occur because of natural seismicity, the primary cause for rockburst events is mining, with geological and geotechnical factors influencing the severity of a rockburst event.

1.1 Brittle shear ratio

The Brittle shear ratio (BSR) is an index used as a tool in the mining industry to assess rockburstability. It was defined by Castro et al. (2012) as a means of determining rock mass damage and its relation to a potential occurrence of strainbursting by using the difference between major and minor principal stress and its relationship with the uniaxial compressive strength (UCS) value, as can be seen in Equation 1.

$$BSR = \frac{\sigma_1 - \sigma_3}{\sigma_c} \quad (1)$$

where:

σ_1 = major principal stress value.

σ_3 = minor principal stress value.

σ_c = uniaxial compressive strength value.

The relationship between the BSR and rockburst events is established in Table 2.

Table 2 Relationship between the value of the brittle shear ratio, rock mass damage and its potential regarding strainbursting (Castro et al. 2012)

BSR	Rock mass damage	Potential for strainbursting
0.35	No to minor	No
0.35 to 0.45	Minor (surface spalling is a potential case)	No
0.45 to 0.6	Moderate (breakout formation expected)	Minor
0.6 to 0.7	Moderate to major	Moderate
>0.7	Major	Major

1.2 Burst potential index

The burst potential index (BPI) is a parameter which describes the ratio between the strain energy stored due to mining and the critical strain energy density value. At first it was defined as a 2D application which considered the mining-induced stresses and energy components related to it (Mitri et al. 1999). Equation 2 shows the calculation of BPI. Khalil (2023) defined a formula to calculate the value of the parameters for a 3D analysis where the strain energy of the rock will depend on the confinement stress (σ_3) and the energy parameter will depend on the state of both the peak principal stress (σ_1) and the confinement stress (σ_3). These equations are shown in Equations 3, 4 and 5.

$$BPI = \frac{ESR}{e_c} \tag{2}$$

where:

ESR = energy storage rate, i.e. the strain energy stored due to mining in a stress-strain curve.

e_c = critical strain energy density value.

For calculation of the energy storage rate, a formula proposed by Vennes et al. (2020) which accounts for the total energy storage rate is presented (Equation 3).

$$ESR_i = 0.5 * \{\sigma_{prin}\}^T{}_i * \{\varepsilon_{prin}\}_i \tag{3}$$

where:

ε_{prin} = principal strain vector.

σ_{prin} = principal stress vector.

Equation 4 shows the calculation for the peak principal stress which is necessary to calculate the critical strain energy density value.

$$\sigma_1^{peak} = \sigma_3 + \sigma_{ci}\left[m_b \frac{\sigma_3}{\sigma_{ci}} + s\right]^a \tag{4}$$

where:

σ_1^{peak} = peak principal stress.

σ_3 = minor principal stress.

σ_{ci} = uniaxial compressive stress of the intact rock.

m_b, s, a = material constants introduced for the generalised Hoek–Brown failure criterion (Hoek et al. 2002).

Equation 5 shows the calculation of the energy density value based on the peak principal stress.

$$e_c = \frac{1}{2E}\left(\sigma_1^{peak\,2} + 2\sigma_3^2 - 2\upsilon\left(2\sigma_1^{peak}\sigma_3 + \sigma_3^2\right)\right) \tag{5}$$

where:

E = Young's modulus of the material

υ = Poisson's ratio of the material.

In the case of BPI, a higher value means a greater potential for bursting.

This paper presents a stepwise methodology for the assessment and safe recovery of a sill pillar at Macassa mine. To assess the stress condition in the pillar, an elastic 3D mine-wide numerical model was created with FLAC3D 7 software (ITASCA 2019). The numerical model employs the Macassa geomechanical database and in situ stress regime. Pillarburst conditions are assessed using the deviatoric stress ratio to estimate potential BSF, and the BPI based on strain energy considerations to examine strainburst potential.

To relate modelled stress conditions and burst-prone rock mass states to support design, the design assessment must consider factors such as the varying susceptibility of excavations to damage, the different damage mechanisms, the interaction of the ground support schemes with the events and the variability of the available data (Mikula 2012). Dynamic support systems have three main parameters: energy absorption capacity, displacement capacity and load capacity.

Ortlepp (1992) proposed an approach for the design of support considering rockburst damage in tunnels. He used energy, tendons, the cladding elements and the extent of the yield as the main steps. In his considerations the design principles are based on the ejection of a single block, closely related to strainburst. Another approach was proposed as a result of the Canadian Rockburst Research Program (1996) after the CAMIRO mining division conducted research on Canadian rockburst events and how the support systems behaved. This approach defined three levels of damage from minor to major. Mikula (2012) developed an empirical chart for the selection of dynamic ground support based on the historical data available at Long-Victor mine.

Based on the literature previously mentioned and other authors (McGarr 1997, Varden et al. 2008) it is necessary to determine the wall damage due to the seismic activity and the related ejection velocity. A good measurement of these components is the energy related to the ejected particle. The kinetic energy considers both the ejection velocity of the particle and the wall damage expressed in the mass of the kinetic energy formula as it was stablished by Guntumadugu (2013). Equation 6 shows the equation for kinetic energy (Ke). The mass can be obtained from numerical modelling while the ejected velocity can be calculated based on the empirical data available from the mine.

$$Ke = \frac{1}{2} * m * v^2 \tag{6}$$

where:

m = mass of the particle ejected

v = velocity of the particle ejected.

2 Case study

The Macassa mine is situated in the town of Kirkland Lake in Ontario, Canada (Figure 1), within the Abitibi greenstone belt. Since its discovery in 1933, Macassa has been a significant gold producer for the country. The operation was suspended in 1999 due to the low gold price but resumed operation in 2002 and later, in 2005, the discovery of the high-grade South Mine Complex (SMC) consolidated the operation.

The current average production rate is 1,000 tonnes per day, with the two main horizons being the historical Main Break and the SMC. The Main Break zone is dipping at 75° while the SMC zone is shallower with a dip of 45°. The predominant mining methods used are overhand and underhand cut-and-fill, with some longhole bulk methods where the conditions are appropriate. All stopes are backfilled, with the majority of the SMC backfilled using paste fill.

This study will consider the sill pillar located on the SMC. The pillar is situated 1,700 m (5,600 ft) below surface. It is 110 m (360 ft) in length and 15.5 m (50 ft) in height, with a varying thickness averaging 3 m (10 ft). As seen in Figure 2, the sill pillar is surrounded by previously mined stopes which are currently backfilled. The main objective of this paper is to assess the stability condition and to support the design of a safe sill pillar recovery. The sill pillar will be extracted with longhole stoping in retreat. To assess the stress condition in the pillar, an elastic 3D mine-wide numerical model has been created with FLAC3D software (ITASCA 2019). The numerical model was based on the Macassa geomechanical database and in situ stress regime evaluation. Pillarburst conditions were assessed using BSR, and the BPI was based on energy considerations. Model calibration relied upon microseismic monitoring activities in the sill pillar over the past year that demonstrated a stable state, which should be reflected on the model to be considered as calibrated.

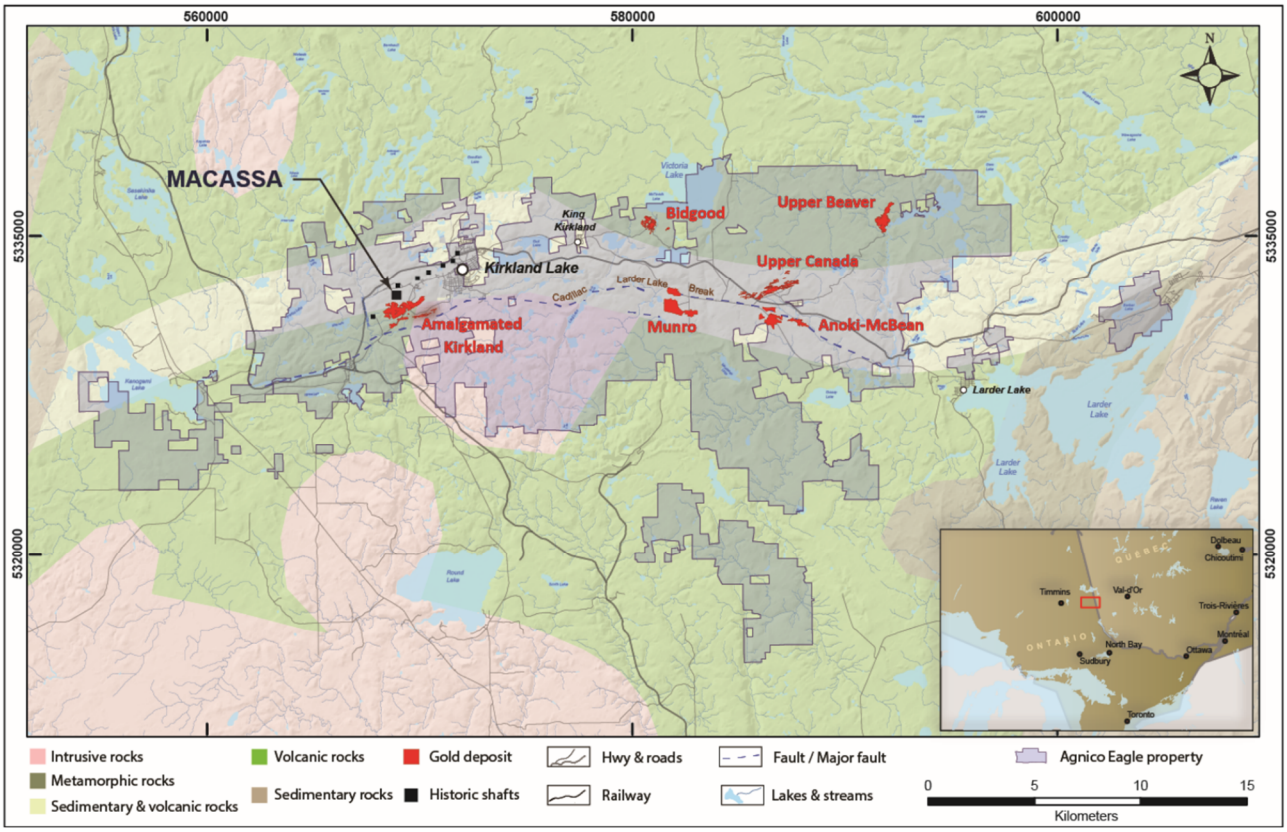

Figure 1 Kirkland Lake Camp — Property and Regional Geology Map, image from Agnico Eagle Mines Ltd

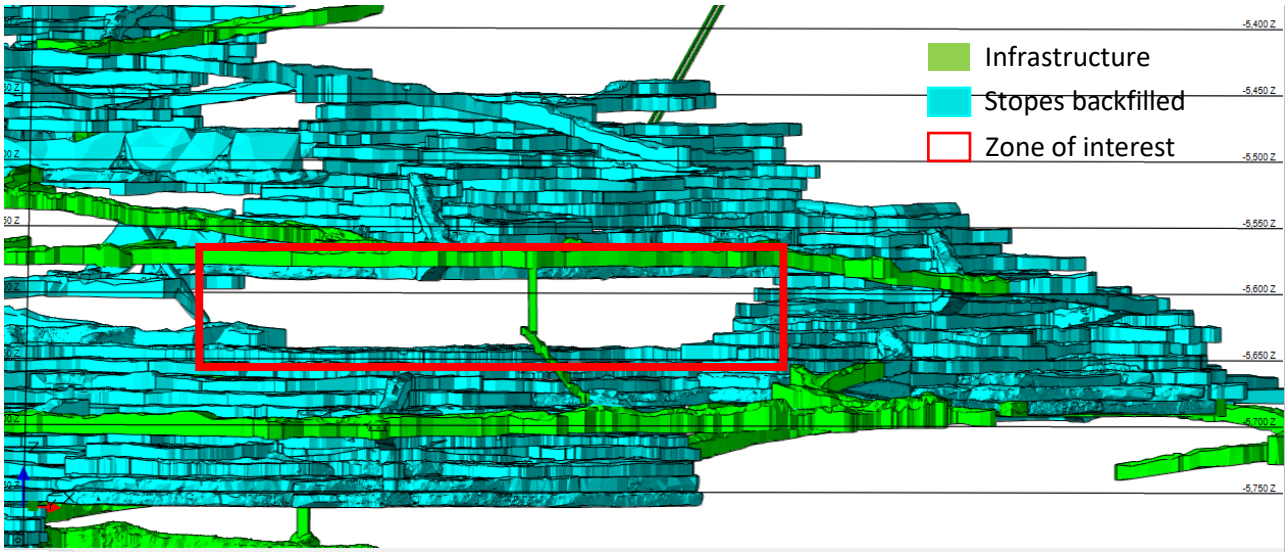

Figure 2 Sill pillar zone view of the South Mine Complex, about 1,700 m (5,600 ft) in depth and surrounded by backfilled stopes

3 Numerical model

A mine-wide model was elaborated to better represent the stress state. The dimensions in each direction are at least five times the measurements of the sill pillar, considering the access and crosscuts related to its exploitation. These dimensions were chosen to assure that the stress state would confidently represent the current stress state of the mine. For this case the dimensions of the sill pillar for the exploitation of the first two stopes of approximately 40 m length and 20 m height were considered (Figure 3). The total dimension of the boundary box is assured to be more than 220 m in the z direction and 880 m in both x and y directions.

Macassa is an interesting case from the perspective of modelling since the stopes are of similar size to the infrastructure due to the main mining method being cut-and-fill. As a result, the effect of mine development is included in the model to measure the stress state.

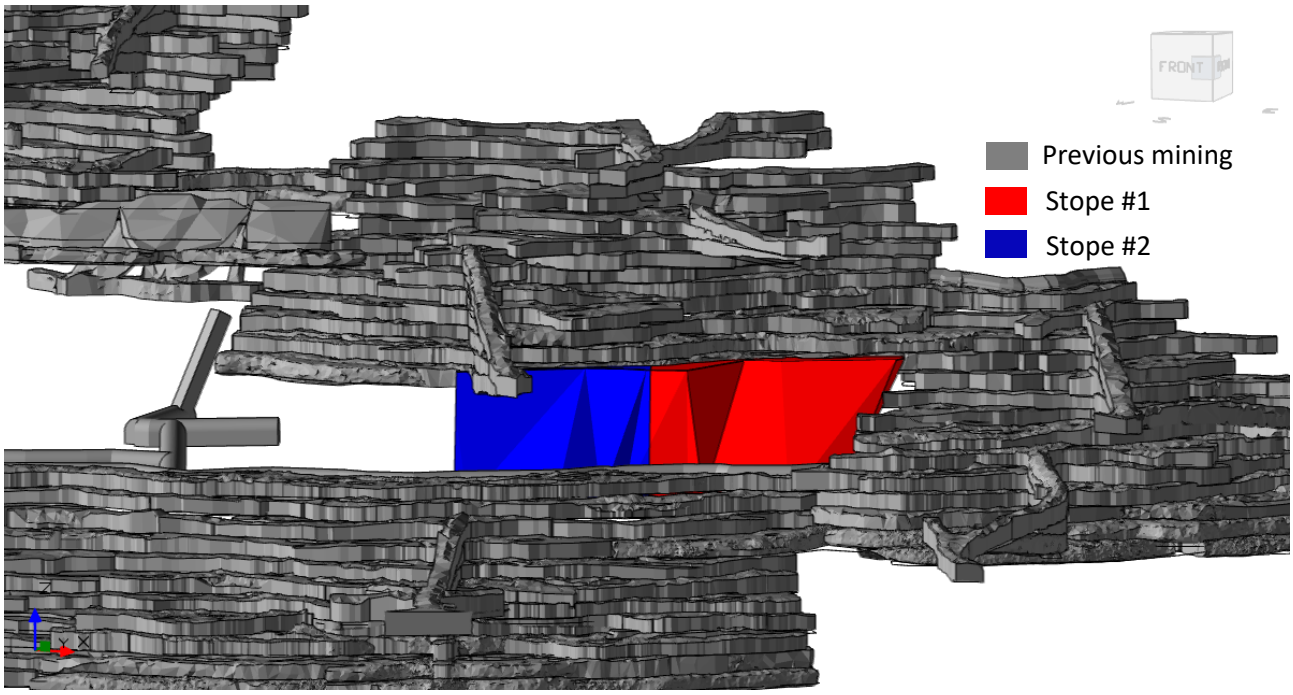

Figure 3 Front view of the stopes located on the sill pillar

For elaboration of the model it was necessary to define the parameters of its construction. With over 2.5 million zones defined, the zone sizes were adjusted depending on whether or not there were any excavations. When there was an excavation nearby the size of the zone was minimised to 1 m. Once the excavation was modelled, a zone of 5 m from the excavation progressively increased its size up to 4 m. Out of this space all the intact zone was modelled to be 8 m.

The grid is composed of cubes with 1 × 1 × 1 m dimensions. Where there was a change in the lithology the cubes were split into smaller cubes to assure the proper classification for the material distribution. Figure 4 shows the different lithologies which were used to represent the distribution of the material properties in the mine. These were based on the latest information provided by the mine. The main properties of the materials are shown in Table 3.

A gravity field stress was assumed and roller boundaries for the horizontal constraints were assumed for the kinematic boundary conditions. A model gravity of 9.8 m/s^2 was assumed but due to the different specific densities there was not a uniform distribution of stress in the vertical direction. For the direction of the principal stress, based on empirical observations made throughout the mine, the major principal stress is assumed to be horizontal and perpendicular to the strike of the structure. In this case the direction of the major principal stress is N45°E.

Six lithologies with different properties have been identified at Macassa. The predominant lithology within the sill pillar is syenite porphyry.

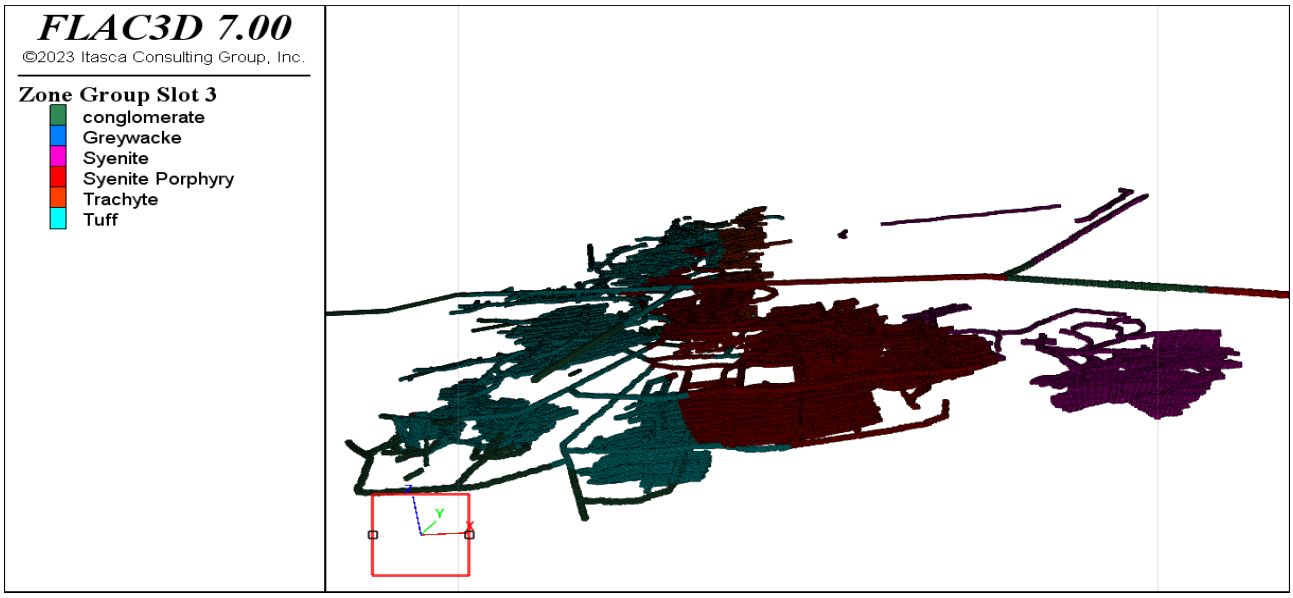

Figure 4 Lithologies available in the zone of the sill pillar

Table 3 Properties of the lithologies of the sill pillar zone used for numerical modelling

Lithology	UCS (MPa)	Density (g/cm^3)	Young's modulus (GPa)	Poisson's ratio
Syenite porphyry	114	2.7	68	0.26
Tuff	154	2.8	72	0.23
Basic syenite	210	2.9	74	0.30
Trachyte	163	2.7	67	0.24
Conglomerate	132	2.7	67	0.24
Greywacke	158	2.7	70	0.26

For the modelling exercise the mining sequence was represented by a sequence of steps where the stress state within the sill pillar was estimated (Figure 5). Model Steps 1 to 9 represent the formation of the sill pillar. Model Steps 10 and 11 represent sill pillar mining, with Step 10 modelling undercut development and Step 11 modelling excavation of the first longhole stope. The stability of Steps 9 to 11 was evaluated with BSR and BPI.

Observations from the field were used to calibrate the model. In Step 9 a stable state of the sill pillar prior to stope extraction is demonstrated by BSR values below 0.6 in the core of pillar, indicating minor rock mass damage with no strainburst potential (as per Castro et al. 2012).

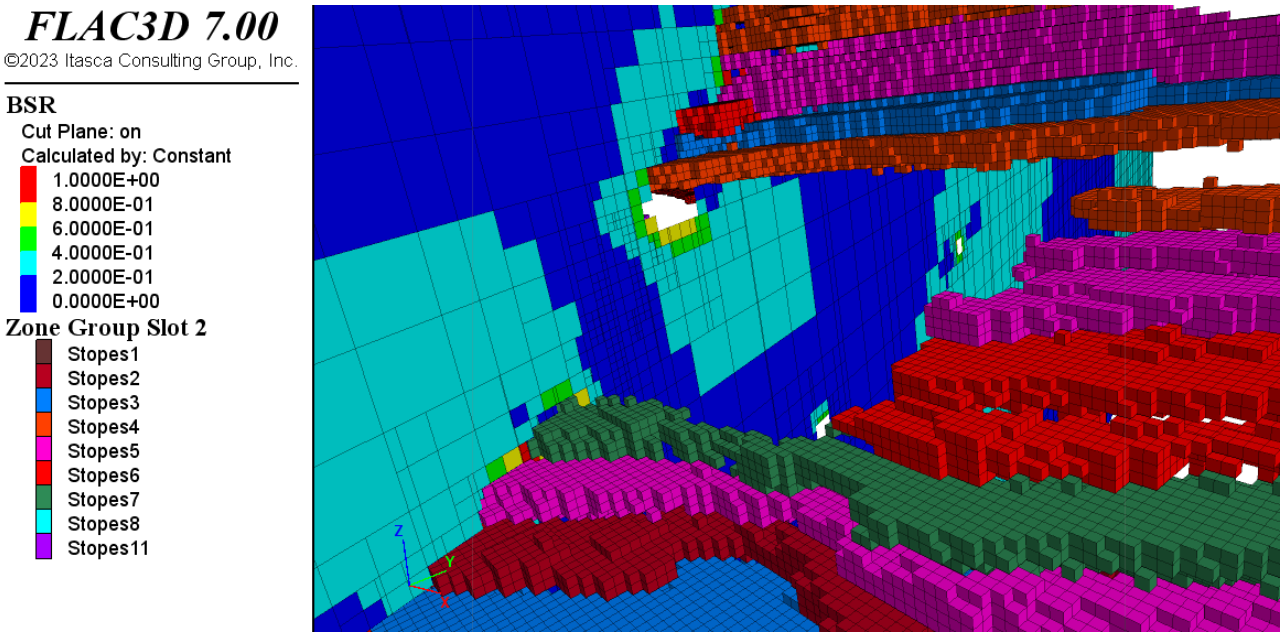

Figure 5 Sill pillar mining sequence geometries constructed in FLAC3D. The plane shows the brittle shear ratio values for Step 11

4 Discussion of results

The pre-sill pillar mining stress state was evaluated in Step 9. Figure 6 shows a BSR plot (UCS 234 MPa) of the sill pillar cross-section and illustrates the core of the pillar, which has a BSR index of 0.2–0.3. According to Castro et al. (2012), a BSR of 0.2–0.3 should correspond to minor rock mass damage and minimal risk of strainbursting. The BPI plot in Figure 7 corresponds with a BPI index of 0–0.1, indicating that the core of the pillar is not prone to strainbursting.

BPI was calculated through post-processing due to a prolonged computation process. Mb, s and a have been determined via various iterations by matching the 'heat map' (BPI > 0.2 from previous events) with observed seismicity of the development.

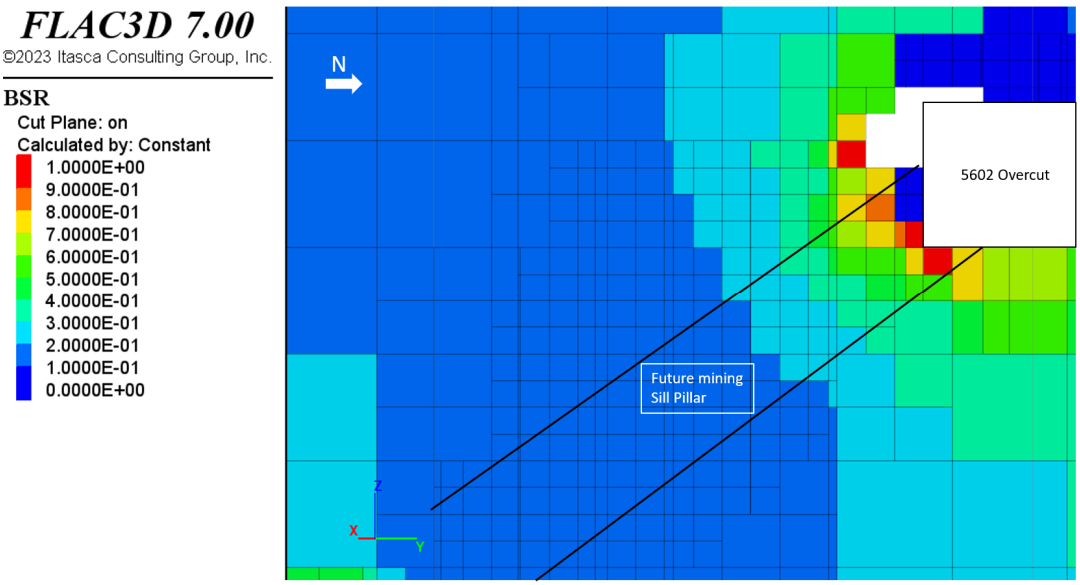

Figure 6 Sill pillar representative cross-section displaying the brittle shear ratio plot for pre-sill pillar mining Step 9

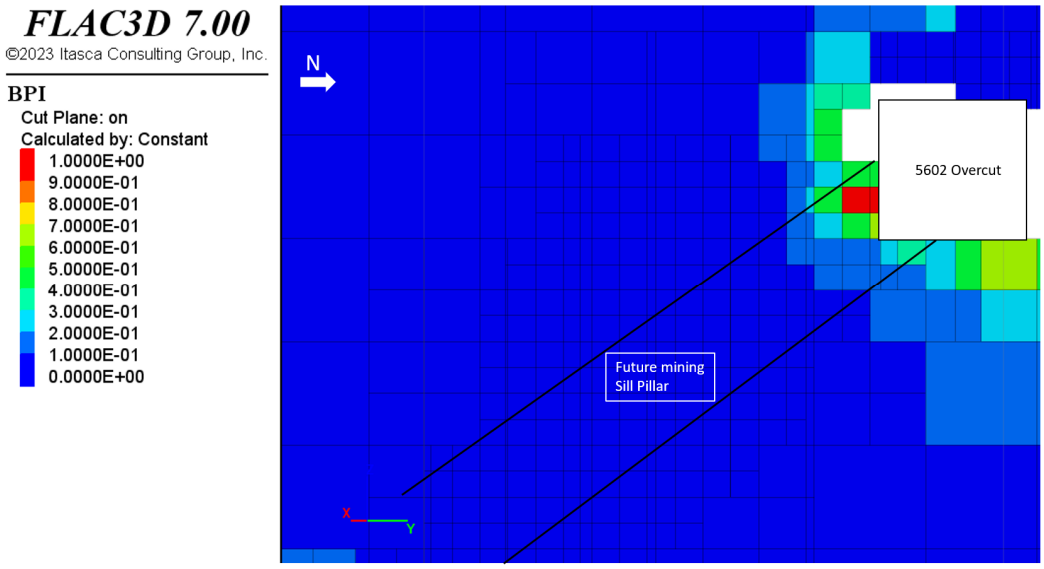

Figure 7 Sill pillar representative cross-section displaying the burst potential index plot for pre-sill pillar mining Step 9

Observations from mining the 5602 overcut concur with the model results. Seismicity was detected in the immediate rock mass surrounding development blasts and minimal seismic events were detected in the core of the pillar. Crews were able to install resin paddle bolts in the back and south wall with some difficulty. Minor seismic shakedown was experienced in the lower south walls following larger moment magnitude events greater than MW0. This damage correlates with the BSR values modelled to be greater than 0.5 surrounding the overcut, indicating moderate damage to the rock mass and burst-prone conditions. Longhole drilling through the core of the pillar has only triggered few, low magnitude seismic events around the collars and toes of the holes. No hole squeezing or crushing has been reported. Harder than usual rock was reported, prompting more frequent bit changes.

The pre-mining stress state was also evaluated at 50% of the average strength to determine BSR sensitivity to UCS values in case of varying rock mass strength along the sill pillar. Changing the UCS to 114 MPa, the BSR index for the core of the sill pillar plots at 0.3–0.4, as seen in Figure 8. This BSR range is still within the Castro et al. (2012) minor rock mass damage rating.

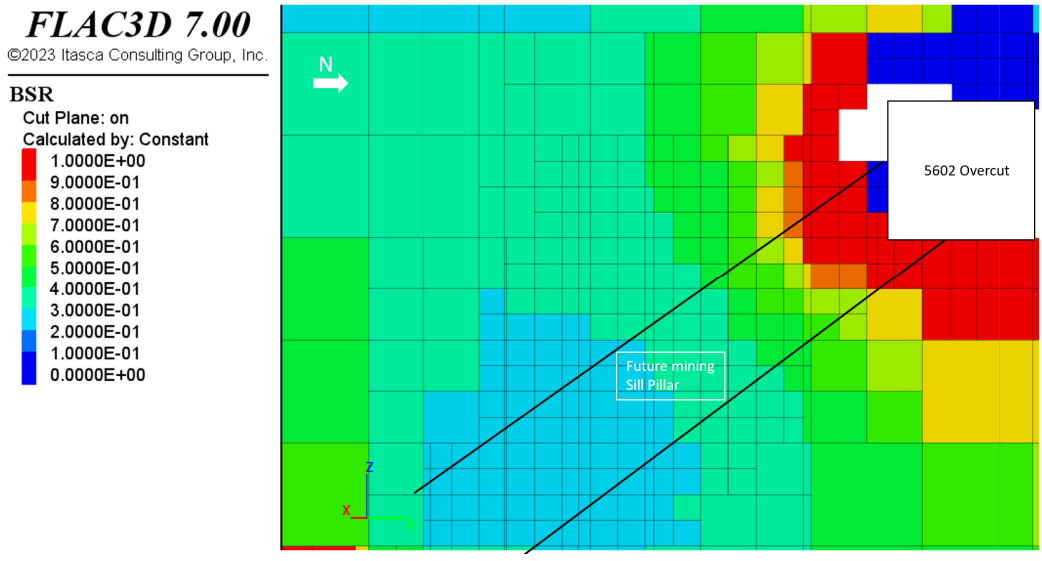

Figure 8 Sill pillar representative cross-section displaying a brittle shear ratio plot for pre-sill pillar mining Step 9 at 50% uniaxial compressive strength strength (UCS) compared to the UCS value used in the calibrated model

Both the BSR and BPI plots at Step 9, with UCS varying from 114–234 MPa, demonstrate that the model calibration for a stable pre-mining sill pillar stress state was achieved. Seismic data and underground observations from development and drilling confirm rock mass conditions are aligned with the BSR and BPI indexes. However, rock mass deformation over time and the resulting stress changes may not be adequately captured by an elastic model. It is necessary to understand how a deteriorating rock mass might change a seismic response that will not be captured by an elastic model. As mining-induced activities such as blasting change the stress regime we can expect increased seismicity in the remaining sill pillar to deteriorate the rock mass, increasing the BSR and BPI indexes and in turn increasing the burst potential. A recommendation for future research is to build an elastic-plastic model which will manage to more accurately represent the stress changes expected from rock mass deformation induced by stope blasting.

In Step 10 the stress state of the sill pillar was evaluated when developing the 5702 undercut using BSR and BPI indexes. Figure 9 shows a BSR plot (UCS 234 MPa) of the sill pillar cross-section. The sill pillar rock mass has progressed to the 0.3–0.4 range and the intact core, with a BSR of 0.2–0.3, has been reduced. The Figure 10 BPI plot illustrates a range of 0–0.1, indicating low strainbursting potential.

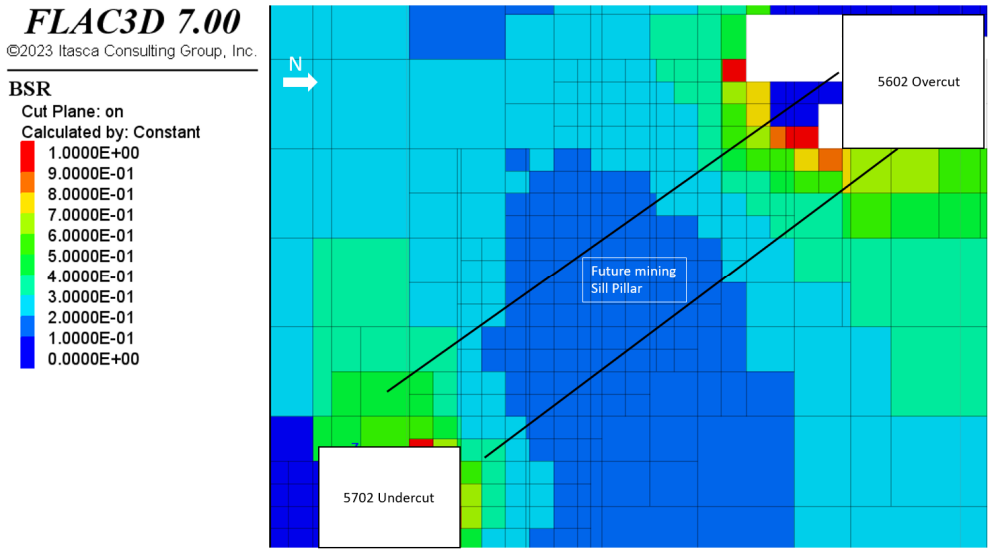

Figure 9 Sill pillar representative cross-section displaying a brittle shear ratio plot for pre-sill pillar mining Step 10

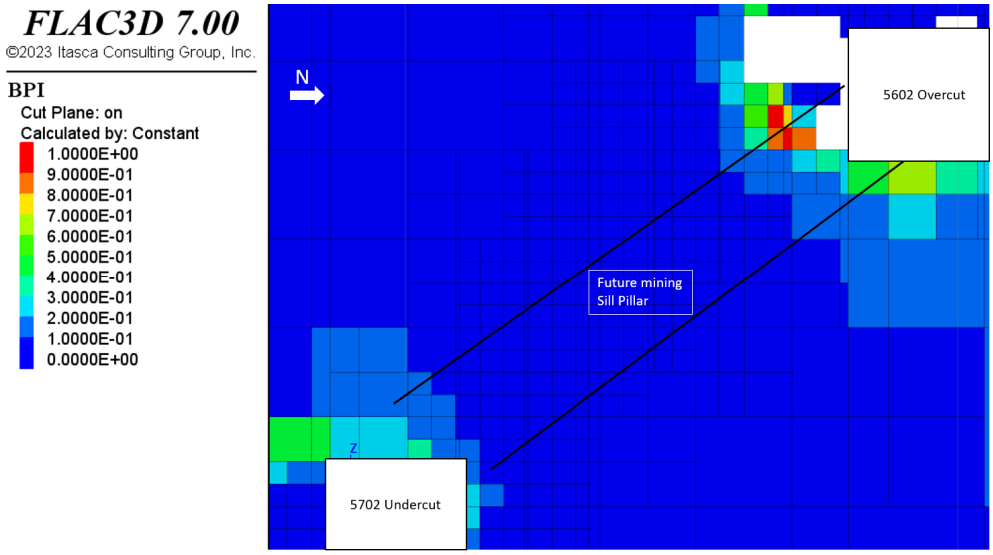

Figure 10 Sill pillar representative cross-section displaying a burst potential index plot for pre-sill pillar mining Step 10

Observations from the undercut concur with the model results. Seismicity triggered by mining and blasting activities was detected in the immediate rock mass surrounding development blasts and minimal seismic events were detected in the core of the pillar. Crews were able to install resin paddle bolts in the back but were not able to install resin bolts in the north wall as the rock mass in the immediate 1–2 m surrounding the excavation has spalled and deteriorated into gravel-like conditions due to the increased induced mining stresses. Elevated post-blast seismicity with seismic events greater than MW0 characterise the seismicity response and stress state of the undercut.

In Step 11 the first sill pillar stope is extracted. Modelled BSR and BPI values indicate the stresses have been redistributed into the adjacent sill pillar longhole stope block, as seen in Figure 11. The intact core of the remaining sill pillar has been reduced significantly and the remaining pillar has a BSR greater than 0.5 and a BPI over 0.3, indicating that Stope 2 mining activities such as drilling and blasting will be more likely to be exposed to burst-prone conditions and seismicity will likely be detected throughout the entire pillar rather than just in the immediate rock mass surrounding the excavations.

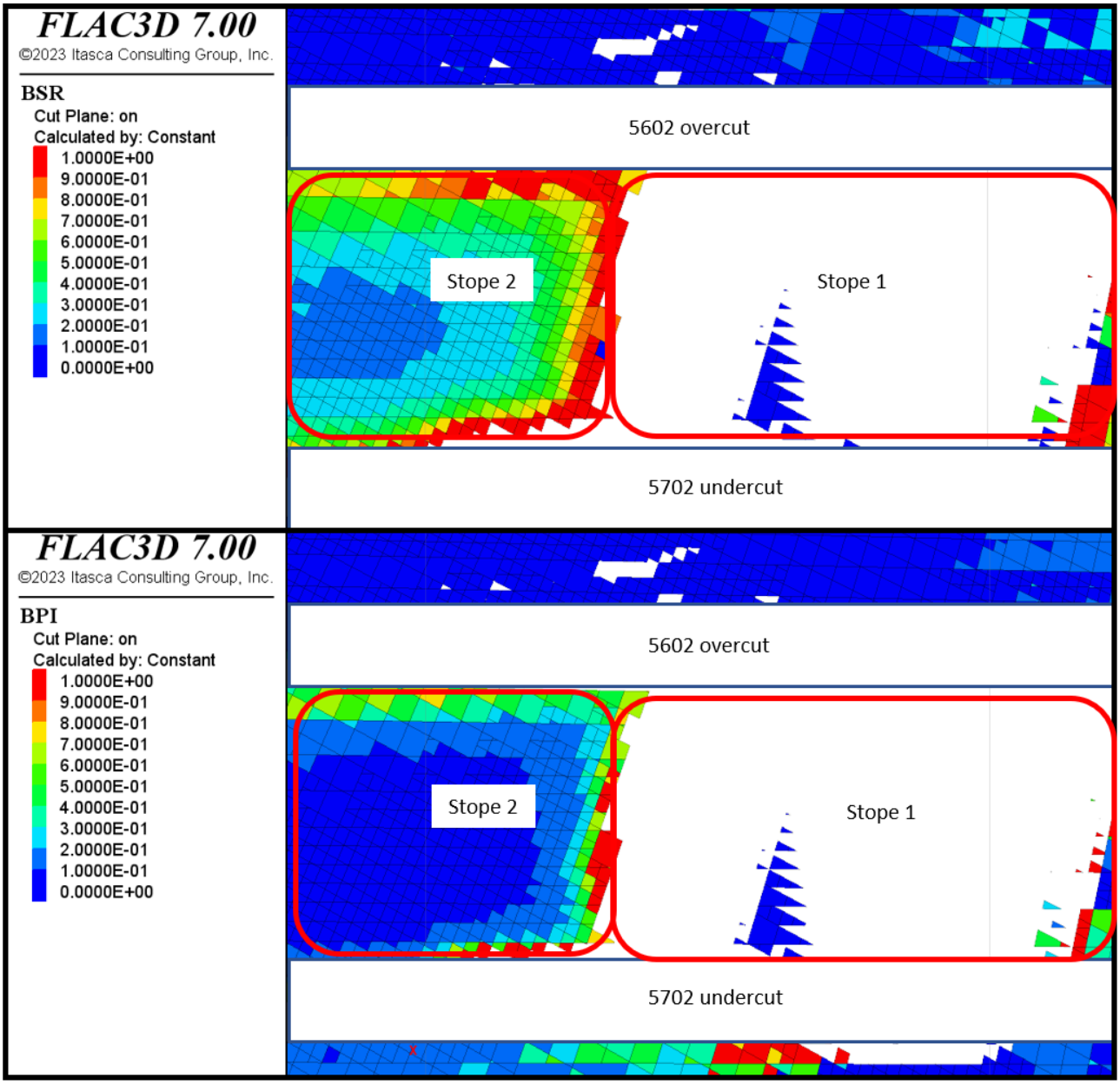

Figure 11 Sill pillar long sections displaying the brittle shear ratio and burst potential index plots for post-Stope 1 blasting mining Step 11

Using the calculated kinetic energy for strainbursts, dynamic support systems can be evaluated against anticipated stress and strainburst conditions. A review of seismic data for the sill pillar area determined the highest value of velocity for an ejected particle is below 1 m/s. Figure 12 illustrates larger magnitude events and their distance from the excavation that was recorded when mining development undercut. These large events were used in particle velocity calculations. For the purposes of conservative energy calculations a value of 1.5 m/s, obtained from the literature review, was assumed to be the critical case. The value of the mass was defined by setting a BSR index threshold of 0.6. For this sill pillar, a threshold BSR value of 0.6 is an appropriate assumption due to the increased likelihood for strainbursting as demonstrated by the model and observed during mining of the overcut and undercut. Using Equation 6 for kinetic energy, a value of 16 KJ/m^2 was calculated to be the dynamic load applied to the ground support system.

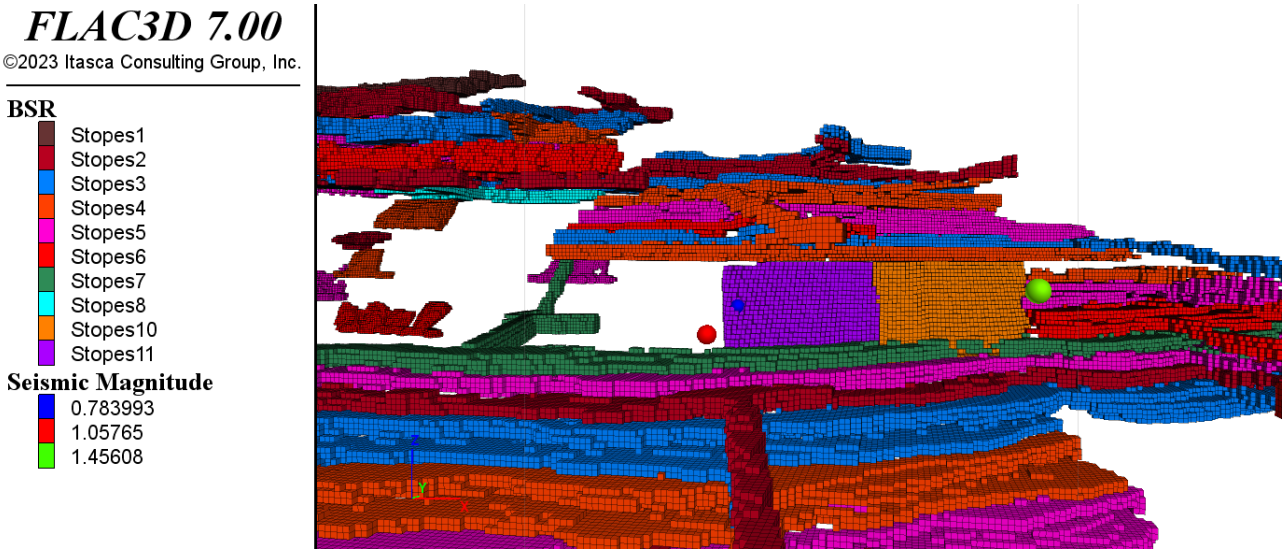

Figure 12 Front view of the stopes. Spheres represent seismic events with a magnitude above 0.5 that were experienced while excavating the undercut

Based on results from the numerical model, the empirical database from the mine and observations in the field, dynamic support was chosen according to the expected micro-seismicity. A representation of the dynamic support chosen for the undercut is shown in Figure 13.

For the overcut, the support selected was as follows:

- 20 mm Versa bolts on 1.22 × 1.22 m (4 × 4 ft) spacing, with dice bolts
- #6-gauge wire mesh screens
- #0-gauge straps on screen seams
- Support to sill/bench elevation
- Arches at intersection about 21 m (70 ft) in all directions.

For the undercut, the support selected was the following:

- 20 mm Versa bolts on 1.22 × 1.22 m (4 × 4 ft) spacing, with dice bolts
- #6-gauge wire mesh screens
- #0-gauge straps on screen seams
- One section primarily supported with MD bolts and re-supported with Versa bolts on the same pattern, without dice bolts.

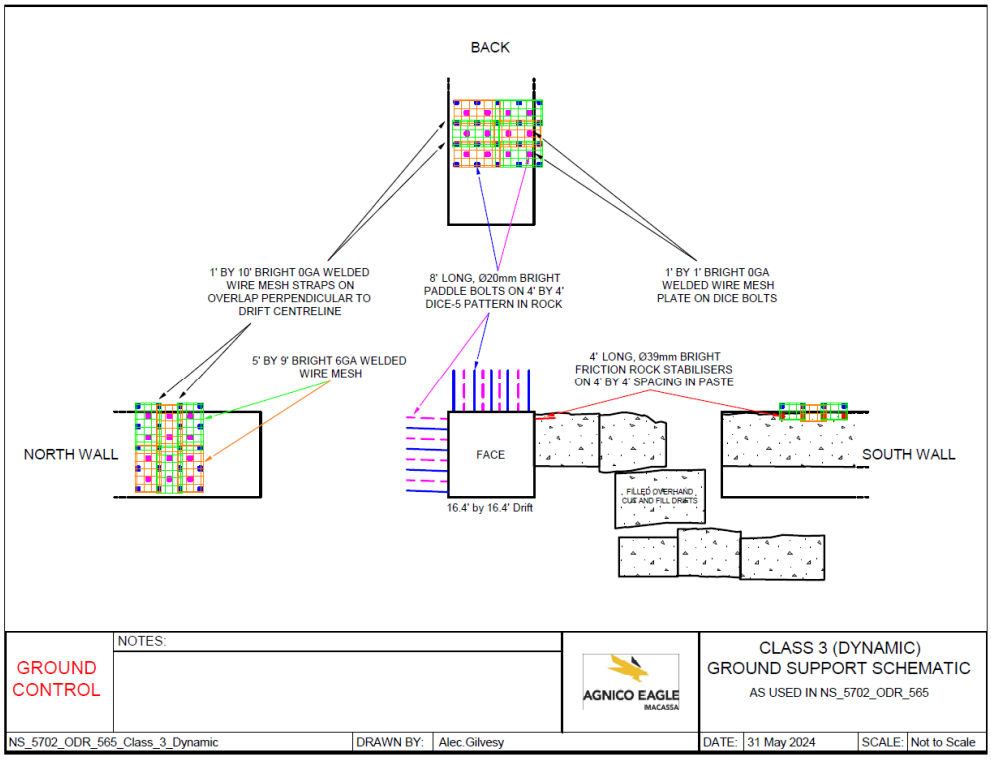

Figure 13 Dynamic support chosen for the undercut of the sill pillar

5 Conclusion

Elastic 3D modelling results demonstrated a stable core pillar during pre-mining and post-blast within the sill pillar. BSR plots indicate that the core of the pillar during overcut and undercut development was below the 0.6 threshold for generating critical particle ejection velocities for this sill pillar case. Higher BSR and BPI values compared to the pillar core were modelled within 2 m of the excavation surfaces but still plotted below the BSR 0.6 and BPI 0.2 thresholds. These results agree with field observations and seismic response from sill development and longhole drilling activities: therefore, BSR and BPI indexes are great indicators for seismic hazard. Derived kinetic energy and dynamic support capacity calculations indicate the current support system in place is appropriate for mining-induced seismicity under current rock mass conditions.

Future modelling work is required to adequately consider the effect of significant rock mass deformation on stress redistribution to the remaining sill pillar once the first stope is blasted. The resultant BSR and BPI index thresholds, and derived kinetic energy calculations, can then be further refined for pillar stability and ground support capacity evaluations. Post-blast reconciliation with future modelling works will be an imperative effort required to evaluate tactical controls in managing seismic risk as sill pillar mining progresses.

These modelling derivations can be used to evaluate the dynamic capacities of ground support systems with the goal of achieving a desired Factor of Safety for expected seismic levels. Support dynamic capacity calculations rely on critical case for kinetic energy per unit of area. This case assumes a higher velocity than the ones found for previous events. Further research on the establishment of the BSR threshold is needed as it is another important aspect of the kinetic energy calculation.

Acknowledgement

We would like to express our sincere gratitude to the Natural Sciences and Engineering Research Council of Canada – NSERC Discovery Program, Grant RGPIN/05645-2020, for its financial support. Additionally, we extend our appreciation to Agnico Eagle Mines Limited for providing valuable information and insights that greatly contributed to the success of this study.

References

Blake, W 1972, 'Rock-burst mechanics', *Quarterly of the Colorado School of Mines*, vol. 67, no. 1, pp. 1–64.

Blake, W & Hedley, D 2003, *Rockbursts, Case Studies from North American Hard-rock Mines*, Society for Mining, Metallurgy and Exploration, New York.

Canadian Rockburst Research Program 1996, *A Comprehensive Summary of Five Years of Collaborative Research on Rockbursting in Hard Rock Mines*, CAMIRO Mining Division, Sudbury

Castro, L, Bewick, R & Carter, T 2012, 'An overview of numerical modelling applied to deep mining', *Innovative Numerical Modelling in Geomechanics*, pp. 393–414.

Gill, D, Aubertin, M & Simon, R 1993, 'A practical engineering approach to the evaluation of rockburst potential', *Proceedings of the 3rd International Symposium on Rockbursts and Seismicity in Mines*, CRC Press, Boca Raton, pp. 63–68.

Guntumadugu, D 2013, *Methodology for the Design of Dynamic Rock Supports in Burst Prone Ground*, PhD thesis, McGill University, Montreal.

He, F 2005, *Study on Geological Hazards in Tunnelling of Deep-Buried Long Tunnels at Ginling-Dabashan Orogen of the Three Gorges Reservoir Water Diversion Project*, PhD thesis, China Academy of Geological Sciences, Beijing.

He, M, Miao, J, Li, D & Wang, C 2007, 'Experimental study of rockburst processes of granite specimen at great depth', *Chinese Journal of Rock Mechanics and Engineering*, vol. 26, no. 5, pp. 865–876.

He, M, Xia, H, Jia, X, Gong, W, Zhao, F & Liang, K 2012, 'Studies on classification, criteria and control of rockbursts', *Journal of Rock Mechanics and Geotechnical Engineering*, vol. 4, no. 2, pp. 97–114.

Hedley, D 1992, *Rockburst Handbook for Ontario Hardrock Mines*, CANMET Special Report SP92-1E, Communication Group, Ottawa.

Hoek, E, Carranza-Torres, C & Corkum, B 2002, 'Hoek-Brown failure criterion – 2002', in R Hammah, W Bawden, J Curran & M Telesnicki (eds), *Proceedings of the Fifth North American Rock Mechanics Symposium (NARMS-TAC)*, University of Toronto Press, Toronto, pp. 267–273.

ITASCA 2019, *FLAC3D — Fast Lagrangian Analysis of Continua in Three-Dimensions*, version 7.0, computer software, ITASCA, Minneapolis.

Kaiser, P & Cai, M 2018, 'Rockburst phenomena and support characteristics', *Rockburst Support Reference Book*, vol. 1, Laurentian University, Sudbury.

Kaiser, P, Tannant, D & McCreath, D 1996, *Canadian Rockburst Support Handbook*, Geomechanics Research Centre, Laurentian University, Sudbury.

Khalil, H 2023, *Effect of Mining and Geology on Induced Seismicity – A Case Study*, master's thesis, McGill University, Montreal.

McGarr, A 1997, 'A mechanism for high wall-rock velocities in Rockbursts', *Pure and Applied Geophysics*, vol. 150, pp. 381–391.

Mikula, PA 2012, 'Progress with empirical performance charting for confident selection of ground support in seismic conditions', in Y Potvin (ed.), *Deep Mining 2012: Proceedings of the Sixth International Seminar on Deep and High Stress Mining*, Australian Centre for Geomechanics, Perth, pp. 71–89, https://doi.org/10.36487/ACG_rep/1201_05_mikula

Mitri, H, Tang, B & Simon, R 1999, 'FE modelling of mining-induced energy release and storage rates', *Journal of the South African Institute of Mining and Metallurgy*, vol. 99, no. 2, pp. 103–110.

Ortlepp, W 1992, 'The design of support for the containment of rockburst damage in tunnels - an engineering approach', *Proceedings of International Symposium on Rock Support in Mining and Underground Construction*, Laurentian University, Sudbury, pp. 593–609.

Ortlepp, W 1997, *Rock Fracture and Rockbursts: an Illustrative Study*, South African Institute of Mining and Metallurgy, Johannesburg.

Solak, T 2009, 'Ground behavior evaluation for tunnels in blocky rock masses', *Tunnelling and Underground Space Technology*, vol. 24, no. 3, pp. 323–330.

Varden, R, Lachenicht, R, Player, J, Thompson, A & Villaescusa, E 2008, 'Development and implementation of the Garford dynamic bolt at the Kanowna Belle Mine', *Tenth Underground Operators' Conference 2008*, Australasian Institute of Mining and Metallurgy, Melbourne.

Vennes, I, Hani, M, Chinnasane, D & Yao, M 2020, 'Large scale destress blasting for seismicity control in hard rock mines: a case study', *International Journal of Mining Science and Technology*, vol. 30, pp. 141–149.